

SOI-CMOS MEMS WALL SHEAR STRESS SENSORS

I. Haneef, S. Z. Ali, F. Udrea,
J. D. Coull, H. P. Hodson

Department of Engineering,
University of Cambridge.

ABSTRACT

This paper presents the results of development work on MEMS-based shear stress sensors and their performance relative to traditional hot film sensors. The devices in question employ micro hot-film sensing elements fabricated using a commercial SOI-CMOS process followed by a DRIE back-etch step. This offers low cost and offers the option of integrating sensor and bridge electronics onto a single chip. The sensing element is aluminium, and is mounted on top of a low thermal conductivity silicon oxide. Two different sizes were manufactured and tested. Compared to standard hot film sensors, these devices have a similar thermal coefficient of resistance but significantly lower power consumption. At a resistive overheat of 0.3, the smaller MEMS devices had a typical cut off frequency of around 120 kHz which was higher than the conventional hot films (45 kHz) and the larger MEMS sensors (29 kHz).

To test the sensitivity, a side-by-side comparison between the larger sensors and conventional hot films was performed on a low speed flat plate rig, the first time such a macro-scale test of MEMS shear sensors has been reported. An array of 16 MEMS sensors and a set of 16 hot films were placed along the length of the plate. The results showed that the MEMS sensors could successfully be used to identify different flow regimes in a comparable manner to the hot film sensors.

A high speed survivability test was carried out in a supersonic wind tunnel to demonstrate that the MEMS sensors are robust enough to be used under these conditions. All the sensors on the test chip survived at Mach 1.2 for the one hour duration of the test.

The calibration and performance of the MEMS devices is discussed with reference to the underlying theory of operation and scope for improving performance is identified.

INTRODUCTION

Thermal anemometry measurements of wall shear stress are typically performed using “macro” scale hot film sensors manufactured by electron beam deposition. Reviews of these techniques are covered in references [1–3]. More recently, research in the MEMS community has produced various MEMS-based shear stress sensors, as reported in references [4–15]. The potential advantages of such devices include their finer resolution and very low power requirements due to small size and the potential for improved high frequency response. Additionally there is the potential to develop fully integrated chips combining sensors and control electronics (as explored in [14] and [15]), doing away with the need for external bridges.

The literature reports MEMS shear stress sensors using various materials for the sensing element (e.g. polysilicon [8, 9, 12, 15], platinum [10], laterally aligned carbon nano tubes (CNTs) [11]) and diverse thermal isolation schemes (e.g. polyimide filled KOH-etched trench [8], surface micro-machined vacuum cavity [9], wafer-bonded vacuum cavity [10] etc). However most of these sensors are not CMOS compatible, and hence pose high manufacturing costs and, in general, do not offer the possibility of circuit integration onto the same chip. Only a few of the sensors reported are CMOS compatible (e.g.[14], [15]) and these too utilize only polysilicon as a sensing element.

This paper reports the performance of novel SOI-CMOS micro hot film shear stress sensors using an aluminium sensing element, and compares them to standard macro hot film sensors. Initial measurements on these sensors were reported in [16]. The CMOS aluminium sensing elements offer the option of on-chip integration with control and read-out electronics and do not suffer from any piezo-resistivity induced pressure sensitivity. Effective thermal isolation of the sensor has been achieved by using the commercially standard DRIE process to form an oxide membrane under the sensing elements.

SENSOR DETAILS

MEMS Sensor Design

The sensors were designed using the standard Cadence™ Virtuoso® custom design platform [17]. Two different sizes of sensor were designed with meander shape aluminium sensing elements mounted in the centre of silicon oxide membrane which provides thermal insulation. This layer was formed by a post CMOS, DRIE back-etch. The larger device had a sensing element of dimensions $130\ \mu\text{m} \times 130\ \mu\text{m}$ mounted on a $500\ \mu\text{m} \times$

500 μm membrane, while the smaller had a $18.5 \mu\text{m} \times 18.5 \mu\text{m}$ sensing element on top of a $266 \mu\text{m} \times 266 \mu\text{m}$ membrane. Fig. 1 shows an optical micrograph of both smaller and the larger MEMS sensors on the substrate alongside a conventional Senflex® hot film sensor.

MEMS Sensor Fabrication

The micro hot-film shear stress sensors were fabricated using a commercial SOI-CMOS process using aluminium metallization for the sensor. After fabrication, the silicon oxide membranes were formed by a DRIE back-etch. Metal alignment marks for the silicon oxide membranes allowed a very accurate back to front alignment and minimized the under cut effect of the DRIE. The typical cold resistance of the sensors is 18Ω for the small sensors and 20Ω for the large sensors, which gives them the advantage of being useable with commercially available constant temperature anemometer bridges. The sensor track is $0.720 \mu\text{m}$ thick. The width and total track length of the sensors is $1.1 \mu\text{m} \times 150 \mu\text{m}$ for the smaller sensor and $3 \mu\text{m} \times 1300 \mu\text{m}$ for the larger.

Hot Film Sensors

The hot films used were 9101 Senflex® sensors manufactured by Tao Systems. The Nickel sensing element is electron beam deposited onto a polyimide substrate. The elements are approximately $1500 \mu\text{m}$ long, $100 \mu\text{m}$ wide and $0.20 \mu\text{m}$ thick.

EXPERIMENTAL SET-UP

Thermal and Electrical Characterization

The temperature coefficient of resistance for the MEMS sensors and conventional hot film sensors was determined by heating a finished wafer on a Signatone® model S-1060R Quietemp DC hot chuck system and measuring the change in sensor resistance with a Keithley® model 2400 source meter. The measurements were made at temperatures from $20\text{--}300 \text{ }^\circ\text{C}$. The sensor I-V characterization was done using a Hewlett Packard 4142B modular DC source/monitor and a Signatone® model S-1160 probe station.

MEMS Sensor Array Packaging

The MEMS sensor chips were wire bonded onto a cavity within PCB strips using a Kulicke & Soffa® model 4123 wedge bonder. The cavities around the sensors were filled with an adhesive to achieve an aerodynamically smooth surface. These PCBs with MEMS sensors were then flush mounted onto a thin aluminium sheet for final mounting in a low speed wind tunnel.

Control Electronics

Both the hot film and MEMS sensors were biased with help of a Dantec Dynamics® model 56C17 constant temperature anemometer (CTA) bridges. These bridges allow an estimate of the sensor frequency response by means of a square wave input. The corresponding responses were captured on an Agilent Technologies® Infiniium model 54810 oscilloscope. For the flat plate tests, a bank of 16 Dantec 56C17 bridges was used to control the sensors.

The resistive overheat ratio α_R is defined as:

$$\alpha_R = (R_{hot} - R_{cold}) / R_{cold} \quad (1)$$

where R_{hot} is the sensor resistance at higher temperature due to joule heating and R_{cold} is the sensor resistance at room temperature. For the calibration runs and the frequency response measurements the overheat ratio was varied between 0.1 and 0.6 for the hot films and between 0.1 and 0.4 for the MEMS sensors.

During the wind tunnel tests the outputs from the bridges were logged at a sampling rate of 60 kHz. A.C. and D.C. components were logged separately with a low-pass filter of 30 kHz to avoid aliasing. The hot films were logged with a resistive overheat of 0.4, and the MEMS sensors at 0.3 (lower because of the limited resistance range of the anemometry bridges). Data was logged for 3 s for both A.C. and D.C. components. Tests were performed at six Reynolds numbers between 50,000 and 500,000 (based on the length of the test section, 0.5 m, and the nominal trailing edge velocity).

Calibration Tunnel

In order to obtain a calibration curve for the MEMS device, a packaged sensor was flush mounted in a calibration wind tunnel, shown schematically in Fig. 2. The tunnel is 50 cm wide, 2.5 cm high and 2.5 m long. Static pressure along the flow direction is measured through tappings which had a spacing of 18 cm along the mid-span of the wind tunnel top wall. The pressure was measured using a PSI 9016 pressure transducer array. The wall shear stress was calculated from the pressure drop along the wind tunnel length, and the sensor output voltage was measured at different resistive overheat ratios and shear stress levels (from 0–1.5 Pa).

Flat Plate Rig

A schematic of the flat plate rig is shown in Fig. 3. This rig has previously been used for a low speed study of unsteady transition in Low Pressure Turbine boundary layers (described in more detail in [19]). The aluminium flat plate is 738 mm long, 458 mm wide and 12.8 mm thick. The leading edge is elliptical with a semi-major axis of 38 mm. For the current study, the nominal trailing edge is fixed at a chord-wise distance of 0.5 m from the leading edge. Symmetric contoured walls above and below the flat plate impose a velocity distribution along the surface. The test section is pressurized by means of an adjustable grid over the exit, and bleed slots are cut into the curved surfaces to avoid flow separation. The approximate velocity distribution, calculated from static pressure measurements, is plotted in Fig. 5 and normalized by the nominal trailing edge velocity. The boundary layer is accelerated up to $S/S_0 = 0.42$ then decelerates. A turbulence grid upstream of the test section induces a free-stream turbulence level of 3% at the plate leading edge.

The MEMS sensors were flush-mounted in a 2 mm thick aluminium insert, shown in Fig. 4, which was installed on top of the existing flat plate test section. Care was taken to taper the edges down to sharp edges to minimize the influence of the installation. The MEMS sensors were located at 40% of the span. An existing set of 16 hot-films are placed at 60% of the span. A photo of the installation, also showing the position of the hot film sensors, is shown in Fig. 6.

High Speed Survivability Test

To provide a measure of the robustness of the MEMS sensors, two chips with several sensors on each were mounted in the working section of a supersonic tunnel for an hour. The free-stream Mach number at the approximate location of the chip was Mach 1.2. Fig. 7 shows the set-up in the working section. The resistance of each sensor on the chip was measured before and after the test to detect any damage.

RESULTS AND DISCUSSION

Temperature Coefficient of Resistance

The effect of temperature on resistance was determined for a large MEMS sensor and a hot film sensor. The results are shown in Fig. 8. The MEMS sensor exhibits a Temperature Coefficient of Resistance (TCR) of 0.319 %/°C (which is higher than those previously reported in literature for micro/nano thermal shear stress sensors) while the hot films exhibit a very similar TCR of 0.341 %/°C.

Thermal Isolation and Power Consumption

The dynamic response of hot film anemometry sensors (on either a macro or micro scale) is highly dependant on the thermal insulation between the sensing element and the material it is mounted on. The Senflex hot film sensors are mounted on polyimide, which has a thermal conductivity of 0.12 Wm-1K, while for the MEMS devices the insulation is provided by a layer of silicon oxide, with a thermal conductivity of around 1.3 Wm-1K. To estimate the thermal isolation of the two sensors current vs. voltage and power vs. temperature characteristics were investigated. The voltage-current characteristics and power vs. temperature rise plot for a large MEMS sensor and a hot film are shown in Fig. 9 and Fig. 10 respectively. The results confirm that the thermal resistance of a MEMS sensor on silicon oxide membrane (i.e. 9488°C/Watt), is more than 15 times better than that for a conventional hot film (i.e. 573°C/Watt). It is further elucidated by Fig 10 that for an input power of 20 mW, the temperature rise of the MEMS sensor is approximately 200°C compared to only 10°C for the hot film sensor. This shows that the MEMS device can operate using a fraction of the power of the standard hot film sensor.

Calibration and Data Reduction: Hot Films v.s. MEMS

Classical shear stress sensor theory relates the power dissipated in a constant temperature sensor to the wall shear stress, as described in [20] and [21]. The flow is considered two-dimensional. The temperature at the surface is at ambient (T_∞) except over a heated length $l = 2L$, where the temperature is T_w . The theory assumes that the thermal boundary layer is thin compared to the heated length. Using an x -axis in the direction of flow and y -axis normal to the surface, the heat transfer in the flow can be adequately modelled by the equation:

$$u \frac{\partial T}{\partial x} = \alpha \frac{\partial^2 T}{\partial y^2} \quad (2)$$

where T is the fluid temperature and α is the thermal diffusivity of the fluid. It is also assumed that the thermal boundary layer is small compared with the velocity boundary layer, and hence the fluid velocity u can be given by the linear relationship:

$$u = \frac{\tau}{\mu} y \quad (3)$$

where τ is the shear stress at the wall and μ is the dynamic viscosity of the fluid. Solving this problem yields the classical result that $Power \propto (ShearStress)^{1/3}$:

$$\frac{P - P_0}{k(T_w - T_\infty)B} = 1.28 \left(\frac{\tau L^2}{\alpha \mu} \right)^{1/3} \quad (4)$$

where k is the thermal conductivity of the fluid, B is the span-wise length of the sensor, P is the power dissipated by the sensor and P_0 is the power dissipated under zero-flow conditions. From this relationship the flow shear stress can be plotted in a semi-qualitative manner as a function of the bridge output voltage for a hot film sensor, in the form of quasi-wall shear stress τ_w [22]:

$$\tau_w = \left(\frac{E^2 - E_0^2}{E_0^2} \right)^3 \quad (5)$$

where E is the measured bridge output voltage and E_0 is its value under zero-flow conditions. This method of data reduction allows the relative magnitude of the shear stress to be compared between sensors without the need for calibration.

For MEMS devices it has been shown that this relationship is not valid because the thermal boundary layer is not small compared to the heated length of the sensor. A two-dimensional model valid for MEMS devices has been proposed in [21]. Strictly speaking this is was for a different design to the current sensors, with a cavity beneath the sensor and membrane. However it is sufficiently close for the purposes of this paper. With this large thermal boundary layer the stream-wise heat dissipation must now be included in the governing equation:

$$u \frac{\partial T}{\partial x} = \alpha \left(\frac{\partial^2 T}{\partial y^2} + \frac{\partial^2 T}{\partial x^2} \right) \quad (6)$$

The solution to this equation is a lot more complex than the classical method in Eq. (4), and does not give a simple power law [21]. Therefore quasi-wall shear stress cannot be plotted in the same manner as for the hot film sensors.

This result adds some complexity to the interpretation of the MEMS data but the problems are not insurmountable. As [21] shows, the calibration is dependant on the dimensionless ratio of conductivity λ which will be fixed for a given sensor design:

$$\lambda = \frac{k_d t}{k L} \quad (7)$$

where k_d is the thermal conductivity of the diaphragm/membrane and t is its thickness.

Although a power law cannot be used for the whole range of the sensor, a power law was found to be a reasonable fit across a limited range of shear stresses, both in previous work ([21]) and the current study. The calibration curve for the larger MEMS sensor (obtained on the calibration tunnel) is shown in Fig. 11, with logarithmic scales, for a resistive overheat ratio of 0.3. This indeed shows that a single power law is not valid across the whole range, since the line is not straight. However for the flat plate experiments Thwaites integral calculations show the approximate range of wall shear stress to be 0 – 0.8 Pa across the measured Reynolds number range. A power law was therefore fitted to this region of the calibration curve and is shown on linear scales in Fig. 12, which shows very close agreement in the desired range. The equation of this line is:

$$\tau = 69.88 \left(\frac{E^2 - E_0^2}{E_0^2} \right)^{1.362} \quad (8)$$

Power is therefore proportional to $\tau^{0.73}$, compared to approximate power laws of $\tau^{0.67}$ and $\tau^{0.85}$ reported for different sensors in [21]. This therefore seems a very reasonable result.

The MEMS measurements were therefore processed as quasi-wall shear stress using:

$$\tau_w = \left(\frac{E^2 - E_0^2}{E_0^2} \right)^{1.362} \quad (9)$$

while the hot film data was plotted as the classical quasi-wall shear stress defined in Eq. (5).

Frequency Response

Theoretical analysis of the bridge electronics and classical analysis of a thin surface-mounted film can be used to obtain a mathematical expression for the cut-off frequency f_{cut} [23]:

$$f_{cut} = \frac{1}{2\pi} \left(\frac{\Omega_n^2 G}{M} \right)^{1/3} \quad (10)$$

where G is the amplifier gain and Ω_n^2 is the natural frequency of the amplifier. This is assumed to be second-order in time and is based on analysis of the circuit shown in Fig. 14 which was analysed by Freymuth [24]. The time constant of the sensor, M , is given by:

$$M = \frac{(1+n)^2}{2n} \frac{R_{hot}}{R_{hot} - R_{cold}} \frac{m_{sensor} c_p}{h A_{sensor}} \quad (11)$$

where n is the ratio of the sensor resistance R_{hot} to R_l (shown in Fig. 14) when the bridge is in balance, and m_{sensor} , c_p and A_{sensor} represent the mass, the specific heat capacity and the surface area of the sensor respectively. Eq. (10) may be rewritten as:

$$f_{cut} \propto \frac{h}{t \rho c_p} \quad (12)$$

where h is the heat transfer coefficient, t is the thickness of the film and ρ is the density of the fluid.

The frequency response and time constants of a hot film sensor can be directly estimated by injecting a sine wave or square wave signal into the CT circuit [24]. The square wave injection method was used to determine the time constant and frequency response for both of the MEMS sensors and the hot film sensors. Typical square-wave responses for all three are plotted in Fig. 13 for an overheat ratio of 0.3. The time constant t_c is the time taken for the signal to return to zero, and the cut-off frequency can be estimated using the relationship from [24]:

$$f_{cut} = \frac{1}{1.5 t_c} \quad (13)$$

Square-wave tests were performed for each of the different sensors at a range of overheat ratios, and the results are plotted in Fig. 15. For an overheat ratio of 0.3, it can be seen that the small MEMS sensor has the highest cut-off frequency (120 kHz), followed by the hot film sensor (45 kHz), and finally the larger MEMS sensors (29 kHz). Fig. 15 also shows that the high frequency response improves with increasing overheat ratio for all three sensors designs. Similar behaviour has been reported previously in [13] and [25] for polysilicon hot-film and nickel hot-wire shear stress sensors, respectively.

Comparative Measurements on the Flat Plate

The flat plate experiment serves to test whether the MEMS sensors have the capability to accurately quantify changes in shear stress and identify the boundary layer state in a low speed flow. This is a test of sensitivity rather than frequency response, since the fluctuations in the flow are all at low frequency (<500 Hz for the data presented here), and hence the larger MEMS sensors were used for these tests.

The data from the flat plate measurements is presented here for a Reynolds number of approximately 170,000. The quasi-wall shear stress (τ_w) for the hot film sensors has been calculated according to Eq. (5), and the MEMS sensors using Eq. (9).

Fig. 16 shows the variation of mean and RMS τ_w along the length of the plate for both the hot films and the MEMS sensors. The broad pattern of the two data sets is largely similar. The mean τ_w drops to around zero as the flow separates at around $S/S_0 = 0.54$, after which both the mean and RMS of the signals increase as the boundary layer undergoes transition to a turbulent state. The different relative τ_w of the turbulent boundary layer between the two sensors could be due to changes in the calibration between turbulent and laminar flow, due to the different nature of laminar and turbulent flows close to the wall.

The raw traces of quasi-wall shear stress obtained on the flat plate using the hot film and MEMS sensor arrays are shown in Fig. 17 and Fig. 18 respectively. The two sets of sensors show a similar pattern. Upstream of $S/S_0 = 0.54$ the flow is laminar and attached. Beyond $S/S_0 = 0.54$, τ_w drops to almost zero and the raw traces in both Fig. 17 and Fig. 18 are flat, indicative of laminar separation. The first disturbances indicative of the start of transition are observed further upstream in the MEMS data (at around $S/S_0 = 0.63$ in Fig. 18) than for the hot film measurements ($S/S_0 = 0.67$ in Fig. 17). This observation agrees with the rises in quasi-shear stress in Fig. 16 which show that transition onset occurs sooner in the MEMS data. This accelerated transition is almost certainly due to the additional disturbances induced by the MEMS insert plate rather than any problem with the sensors themselves.

The signal-to-noise ratio was estimated for both the hot film and MEMS data. The RMS of the voltage trace in zero flow was superimposed onto the voltage change measured in the experiment, and the impact on quasi-wall shear stress was estimated. For the first film in each array, this gave a signal-to-noise ratio of 9.7 for the hot films and 6.5 for the large MEMS sensors.

Overall, this comparison with the hot film data shows that in spite of the order of magnitude reduction in size, the current large MEMS sensors perform reasonably well compared to the existing hot film technology in this low-speed flow.

High Speed Survivability Test

The resistances of the sensor on the test chip measured before and after the high speed run did not change, showing that the sensors are robust enough to withstand supersonic flow conditions. A visual inspection under a microscope was also conducted and showed the membranes to be undamaged.

FUTURE WORK

Further improvements in sensor design and materials should allow a large improvement in performance, particularly the frequency response. Eq. (12) shows that the cut-off frequency is inversely proportional to specific heat capacity of the sensing element. For aluminium, this has a value of $900 \text{ Jkg}^{-1}\text{K}^{-1}$. A tungsten element ($c_p = 134 \text{ Jkg}^{-1}\text{K}^{-1}$) should therefore provide a much higher cut off frequency. In addition, because of its very high melting point ($3410 \text{ }^\circ\text{C}$) it should be possible to operate tungsten sensors at a higher overheat ratio which will further improve the sensitivity and improve the high frequency response.

The sensors also need to be tested under supersonic flow conditions, which would provide a more challenging test of the frequency response.

CONCLUSIONS

In this work, we have compared the performance characteristics of novel, high performance MEMS thermal wall shear stress sensors with standard hot film sensors. The findings can be summarised as follows:

1. The MEMS devices were found to exhibit similar thermal properties to the hot films.
2. The MEMS devices operate at much lower power than the hot films, which makes them more suitable for applications requiring low power and wireless sensing.
3. The MEMS devices do not follow the classical result that $power \propto (shear\ stress)^{1/3}$. Calibration of one sensor showed that a power law fit of $power \propto (shear\ stress)^{0.73}$ was appropriate for low values of shear stress.
4. The smaller MEMS device had a better frequency response than the hot film sensors, while the larger MEMS device performed more poorly across the range of overheat ratios tested.
5. The MEMS devices are sufficiently robust to withstand supersonic flow conditions.
6. There is scope for improving the current design of sensor, in particular improving the high frequency response.

ACKNOWLEDGMENTS

I. Haneef thanks Higher Education Commission of Pakistan for support of this work through its Overseas PhD Scholarship Program. Technical help of Dr Davor Dukic in fabrication of PCBs for the MEMS sensors and help provided by Dr Rob Miller in packaging of MEMS sensor for calibration test rig is also gratefully acknowledged.. Thanks are also due to the Whittle Laboratory technical staff.

REFERENCES

- [1] T. J. Hanratty and J. A. Campbell, "Measurement of Wall Shear Stress," in Fluid Mechanics Measurements, 2nd ed., R. J. Goldstein Ed., Taylor & Francis, USA, 1996, pp. 575–648.
- [2] J. H. Haritonidis, "The Measurement of Wall Shear Stress," in Advances in Fluid Mechanics Measurements, M. Gad-el-Hak Ed., Springer-Verlag, 1989, pp. 229–261.
- [3] K. G. Winter, "An outline of the techniques available for the measurement of skin friction in turbulent boundary layers," Prog. Aeronaut. Sci., vol. 18, pp. 1–57, 1977.
- [4] L. Löfdahl, and M. Gad-el-Hak, "MEMS based pressure and shear stress sensors for turbulent flows," Meas. Sci. Technol., vol. 10, pp. 665–686, 1999.
- [5] L. Löfdahl, and M. Gad-el-Hak, "MEMS applications in turbulence and flow control," Prog. Aerospace Sci., vol. 35, pp.101–103, 1999.
- [6] J. Naughton, and M. Sheplak, "Modern developments in shear-stress measurement," Prog. Aero. Sci., vol. 38, pp. 515–570, 2002.
- [7] M. Sheplak, L. Cattafesta, and T. Nishida, "MEMS Shear Stress Sensors: Promise and Progress," AIAA 2004-2606, Proc. 24th AIAA Aerodynamic Measurement Technology and Ground Testing Conference, Portland, OR, 28 Jun –1 Jul, 2004.
- [8] E. Kälvesten. "Pressure and wall shear-stress sensors for turbulence measurements," thesis, KTH, Sweden, 1996.
- [9] C. Liu, C-B. Huang, Z. Zhu, F. Jiang, S. Tung, Y-C. Tai and C-M. Ho, "A micromachined flow shear-stress sensor based on thermal transfer principles," J. Microelectricalmech. Syst., vol. 8, pp. 90–99, 1999.
- [10] M. Sheplak, V. Chandrasekaran, A. Cain, T. Nishida, and L. Cattafesta, "Characterization of a micromachined thermal shear-stress sensor," AIAA J., vol. 40, pp. 1099–1104, 2002.

XIX Biannual Symposium on Measuring Techniques in Turbomachinery
Transonic and Supersonic Flow in Cascades and Turbomachines

- [11] S. Tung, H. Rokadia, and W. J. Li, "A micro shear stress sensor based on laterally aligned carbon nanotubes," *Sensors and Actuators A: Physical*, vol. 133, pp. 431–438, 2007.
- [12] M. Kimura, S. Tung, J. Lew, C-M Ho, F. Jiang, and Y-C Tai, "Measurements of wall shear-stress of a turbulent boundary layer using a micro-shear-stress imaging chip," *Fluid. Dyn. Res.*, vol. 24, pp. 329–342, 1999.
- [13] J-B Huang, Z. Zhu, F. Jiang, Y-C Tai, and C-M Ho, "A microelectro-mechanical-system-based thermal shear-stress sensor with self-frequency compensation," *Meas. Sci. Technol.*, vol. 10, pp. 687–696, 1999.
- [14] X-Q. Wang, Z. Han, F. Jiang, T. Tsao, Q. Lin, Y-C. Tai, V. Koosh, R. Goodman, J. Lew, and C-M. Ho, "A fully integrated shear-stress sensor," *Proceedings of Transducers 99*, pp. 1074–1077, 1999.
- [15] Y. Xu, Y-C Tai, A. Huang and C-M. Ho, "IC-integrated flexible shear-stress sensor skin," *J. Microelectromech. Syst.*, vol. 12, pp. 740–747, 2003.
- [16] I. Haneef, S. Z. Ali, F. Udrea, J. D. Coull, H. P. Hodson, "High Performance SOI-CMOS Wall Shear Stress Sensors," *Proc IEEE Sensors 2007*, pp 1060-1064, 2007
- [17] http://www.cadence.com/products/custom_ic/index.aspx
- [18] S. M. Allameh, "Silicon based microelectromechanical systems," in *Advanced Structural Materials; Properties, Design Optimization and Applications*, W.O. Soboyejo and T. S. Srivatsan Ed., CRC Press, Taylor & Francis Group, USA, 2007, pp. 70.
- [19] J. D. Coull, R. L. Thomas, and H. P. Hodson, "Velocity Distributions for Low Pressure Turbines," *ASME paper GT2008-50589*, 2008
- [20] R. J. Goldstein, "Fluid Mechanics Measurements" Hemisphere Publishing Corporation, London, 1983
- [21] Q. Lin, F. Jiang, X-Q. Wang, Y. Xu, Z. Han, Y-C. Tai, J. Lew, C-M. Ho, "Experiments and Simulations of MEMS Thermal Sensors for Wall Shear Stress Measurements in Aerodynamic Control Applications", *Journal of Micromechanics and Microengineering* 14 pp. 1640-1649, 2004
- [22] H. P. Hodson, "The Detection of Boundary Layer Transition and Separation in High Speed Turbine Cascades," *Measurement Techniques for Transonic and Supersonic Flow – Proc. 7th Symposium, Aachen, 21-23 Sept 1983*
- [23] S. Gjerstad, Y. Fu, H.P. Hodson, W.N. Dawes, D.F. Moore, "A Study of the Frequency Response of a Micro Machined Shear-Stress Sensor Based on Thin Film Anemometry" *Measuring Techniques in Transonic and Supersonic Flows in Cascades and Turbomachines, Proc. 15th Symposium, Florence, 21-22 Sept 2000*
- [24] P. Freymuth, "Frequency-response and electronic testing for constant-temperature hotwire anemometers," *J. Phys. E: Sci. Instr.*, vol.10, pp. 705–710, 1977.
- [25] U. Buder, A. Berns, E. Obermeier, R. Petz, and W. Nitsche, "Aero- MEMS wall hot-wire anemometer on polyimide foil for measurement of high frequency fluctuations on curved surfaces," *Proc. 4th IEEE Sensors Conference*, Irvine, CA, USA, October 31- November 3, 2005, pp. 545–548, ISBN: 0-7803-9057-1.

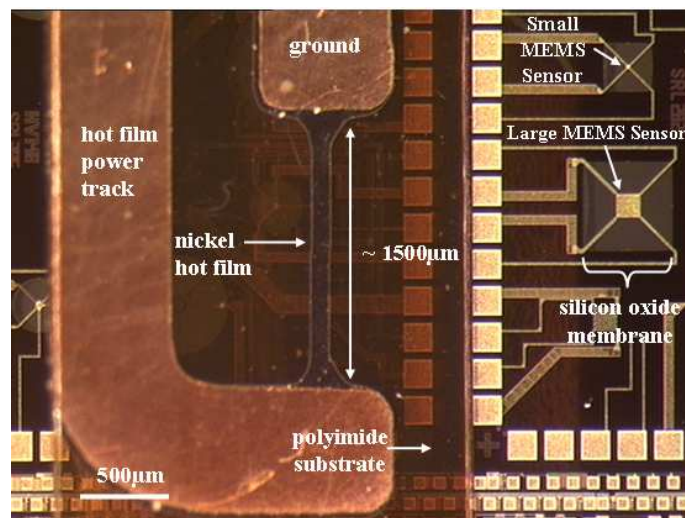


Fig. 1 A large MEMS sensor alongside a conventional Senflex hot film sensor

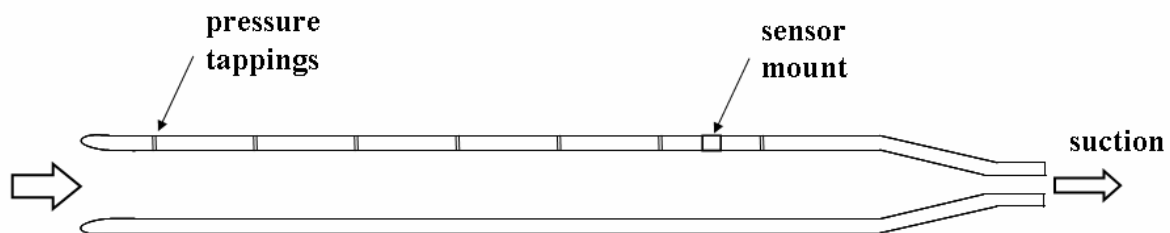


Fig. 2 Schematic of the two-dimensional calibration tunnel

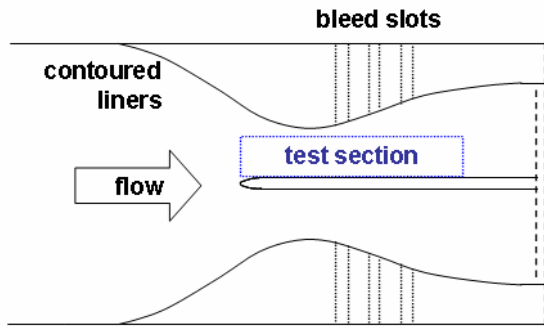


Fig. 3 Schematic of the flat plate rig

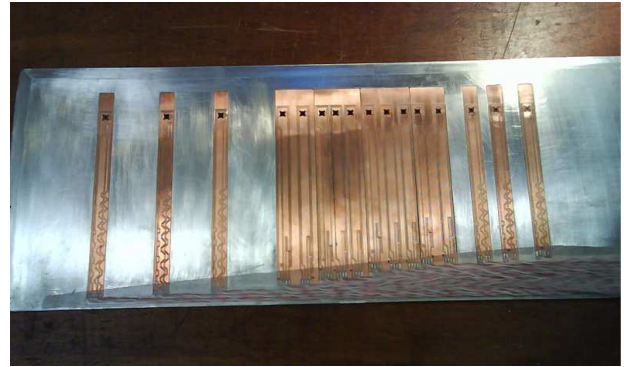


Fig. 4 The insert with the MEMS devices

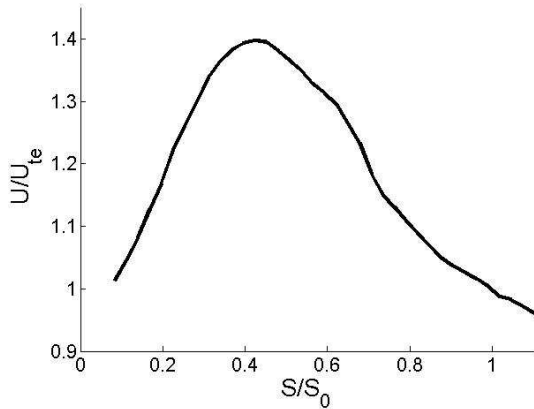


Fig. 5 Approximate velocity distribution along the flat plate (measured without insert) for $Re = 270,000$

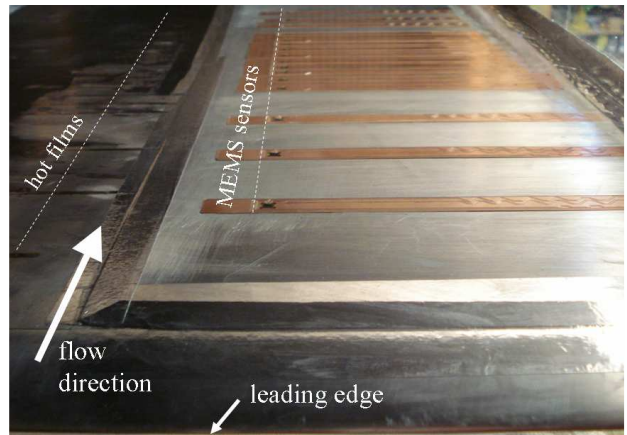


Fig. 6 The insert installed on the flat plate rig, showing the location of the hot films and MEMS sensors

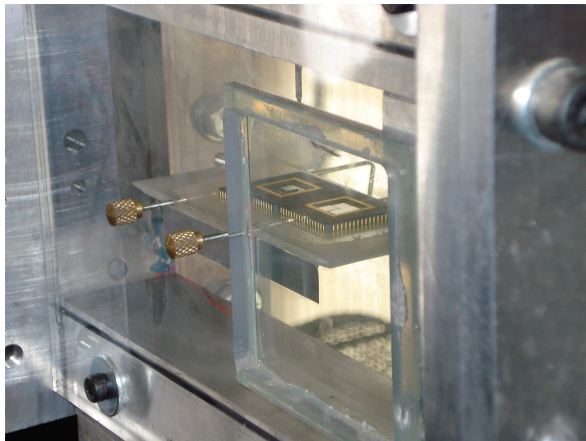


Fig. 7 The installation of the MEMS sensor chips on the high-speed tunnel

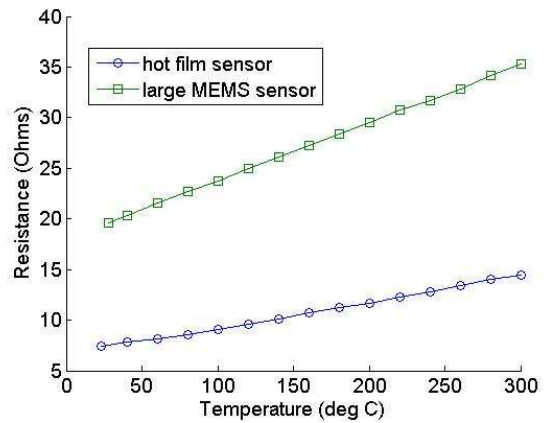


Fig. 8 The effect of temperature on the resistance of a hot film sensor and a large MEMS sensor

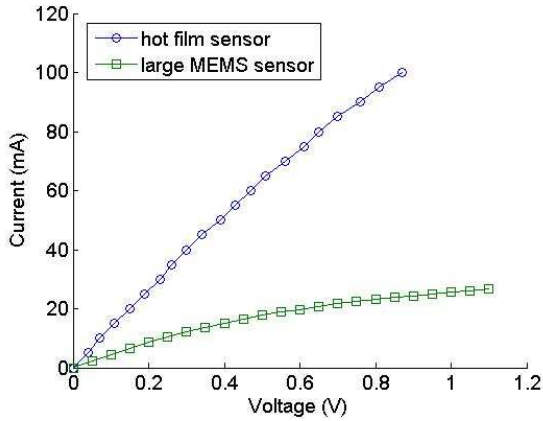


Fig. 9 Comparison of I-V characteristics of a hot film sensor and a large MEMS sensor

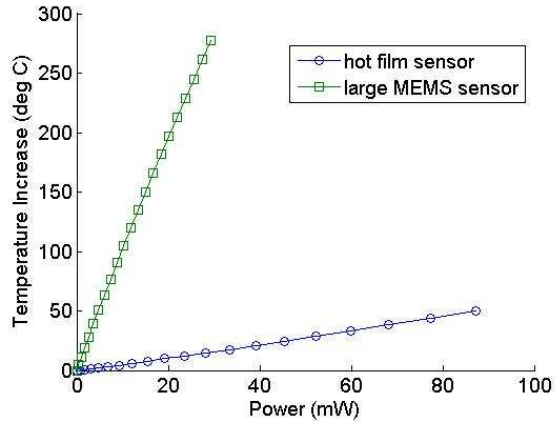


Fig. 10 Comparison of temperature rise at various power inputs for a hot film sensor and a large MEMS sensor

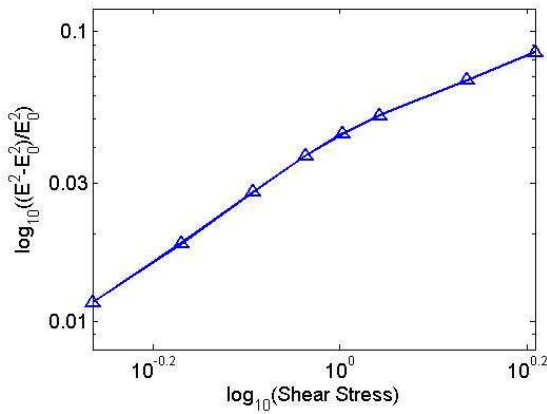


Fig. 11 Calibration data for a large MEMS sensor with a resistive overhear ratio of 0.3

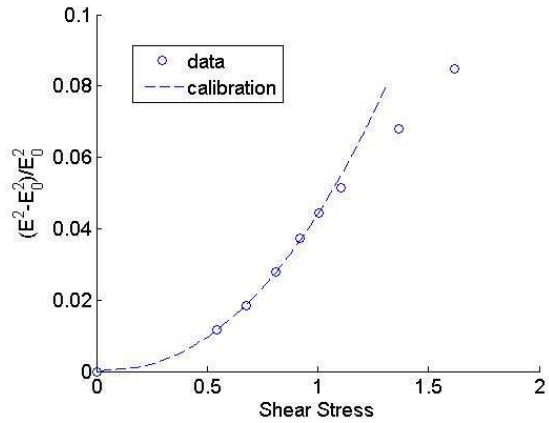


Fig. 12 Calibration curve for large MEMS device, for Shear Stress < 0.8 Pa:

$$Shear\ Stress = 69.9 \left(\frac{E^2 - E_0^2}{E_0^2} \right)^{1.362}$$

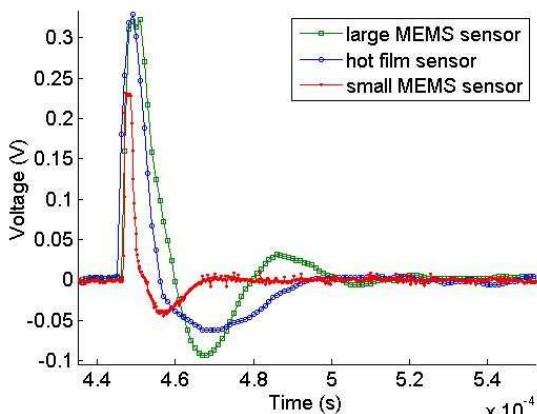


Fig. 13 Typical square-wave response signals for a hot film and the two MEMS sensor at a resistive overhear ratio of 0.3

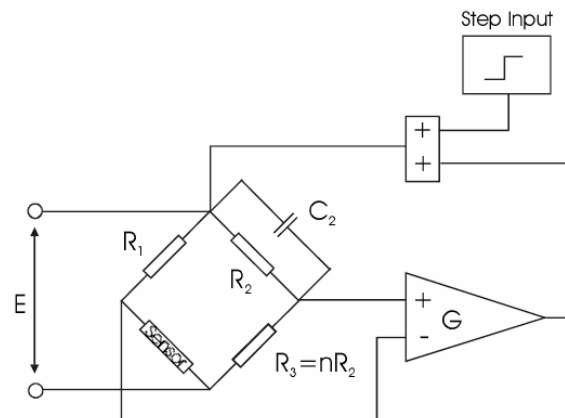


Fig. 14 Bridge Circuit for frequency analysis used in [22] and [24]

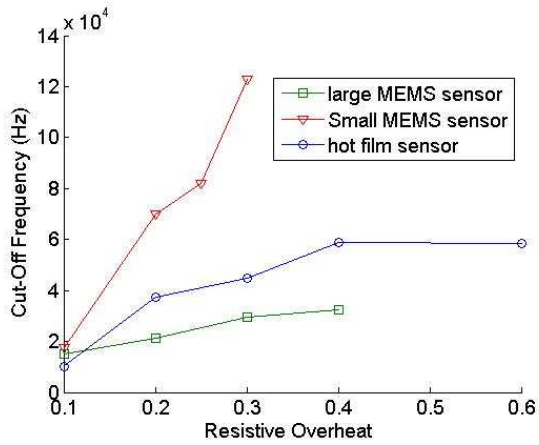


Fig. 15 The effect of overheat ratio on the cut-off frequency of each sensor

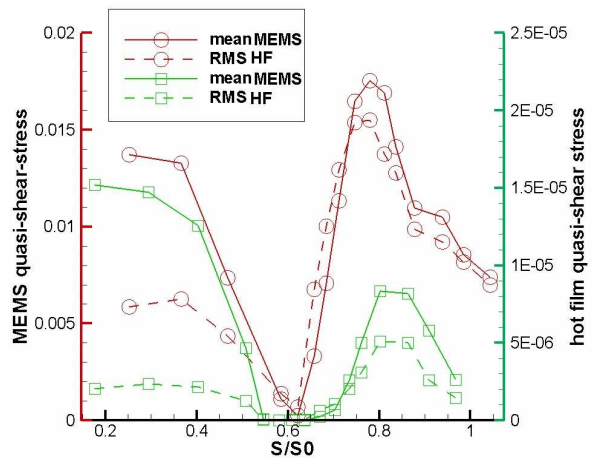


Fig. 16 Variation of mean and RMS quasi-wall shear stress on the flat plate, $Re \approx 170,000$

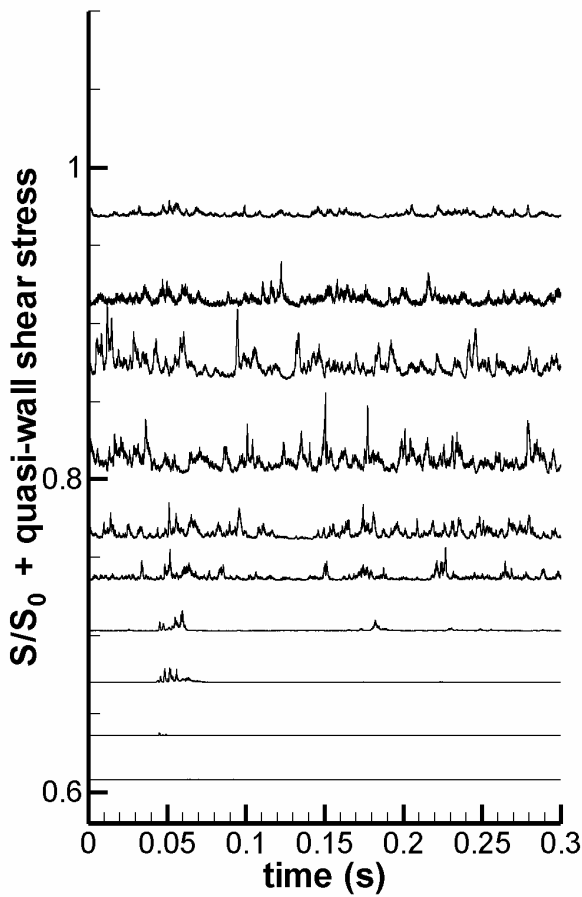


Fig. 17 Raw traces of quasi-wall shear stress obtained with hot films, $Re \approx 170,000$

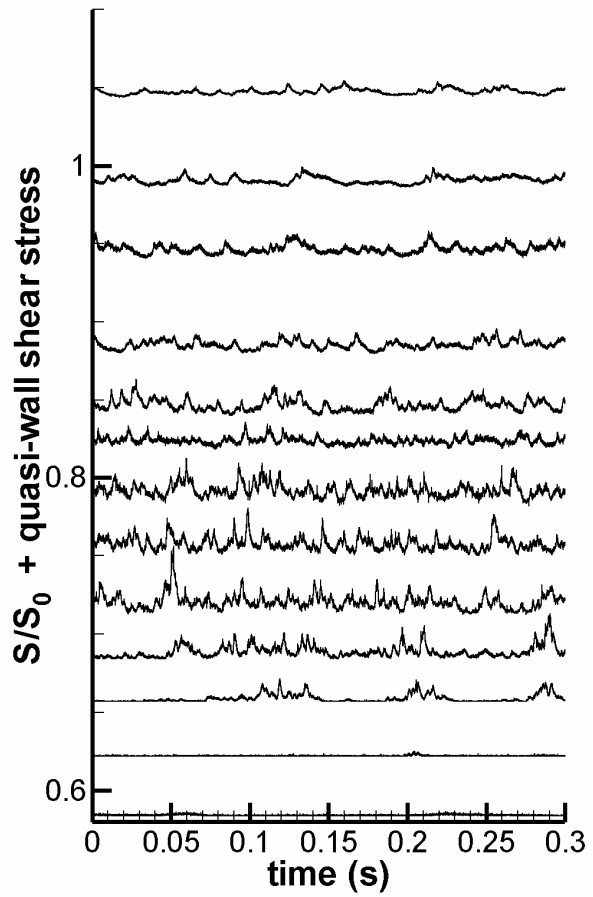


Fig. 18 Raw traces of quasi-wall shear stress obtained with large MEMS devices, $Re \approx 170,000$